Facile Synthesis of Nano-Diced SnO$_2$–ZnO Composite by Chemical Route for Gas Sensor Application

K.S. PAKHARE,[1,2] B.M. SARGAR [ID],[1,6] S.S. POTDAR,[3] A.K. SHARMA,[4] and U.M. PATIL[5]

1.—DIST-FIST Sponsored Material Research Laboratory, Department of Chemistry, Jaysingpur College, Jaysingpur, Tal- Shirol, Kolhapurx, MS 416101, India. 2.—Anandibai Raorane Arts, Commerce and Science College, Vaibhavwadi, Sindhudurg, MS 416810, India. 3.—Department of Physics, Sanjivan Engineering and Technology Institute, Panhala, Kolhapur, MS 416201, India. 4.—School of Physics, Shree Mata Vaishno Devi University, Kakryal, Katra, JK 182301, India. 5.—Department of Physics, Center for Interdisciplinary Research Study, D.Y. Patil University, Kolhapur, MS 416006, India. 6.—e-mail: sargarbalasaheb@gmail.com

The simple chemical bath deposition (CBD) method is used to synthesize SnO$_2$–ZnO nanocomposite at room temperature. Formation of SnO$_2$–ZnO nancomposite is confirmed by the x-ray diffraction (XRD) pattern of annealed films. Scanning electron microscopy (SEM) micrographs of nanocomposite SnO$_2$–ZnO depict that morphological change from nanocubes to manifold hexagonal nanorods with an increase in ZnO content in a composite sample. Also, pure SnO$_2$ sample exhibits interconnected nanospheres. Electron dispersive spectroscopy (EDS) is employed to confirm elemental compositions in composite films. SnO$_2$–ZnO samples were applied as a sensor for different test gases, namely liquified petroleum gas (LPG), ethanol, ammonia (NH$_3$), and hydrogen sulfide (H$_2$S). The maximum response of 59.67% is observed for ethanol at an operating temperature of 275°C and 24 ppm gas concentration. Also, a composite sensor shows a quick response in comparison with a bare sensor. This superior performance of composite over pure sensor may be attributed to a n–n heterojunction at intergrain boundaries. The SnO$_2$–ZnO sensor is found to be selective towards ethanol even at lower gas concentrations.

Key words: Chemical bath deposition method, XRD, SEM, gas sensor

INTRODUCTION

Nowadays, solid-state gas sensors are mostly operative tools to detect a concentration of toxic, hazardous, pollutant and combustible gases in atmospheres. Such solid-state semiconductor gas sensors based on metal oxides have been widely used. The n-type material with relatively little oxygen adsorption sites available is suitable for sensing application due to a created range of a conduction barrier such as zinc oxide (ZnO) and tin oxide (SnO$_2$).[1,2] Many other oxides like CdO, In$_2$O$_3$, WO$_3$, ZnO, SnO$_2$ and CeO$_2$, have been examined to enhance the sensitivity, gas response and selectivity[3–9] Besides this, stability of material, cheapness, controlled industrial use of gas sensor devices and gas response at lowermost operating temperature conditions are the big challenges in this field. Recently, nano-composites are attracting attention to overcome such problems. Such type of sensors were suggested to improve thermal properties since they contain many heterogenous interfaces between different phases reliability ZnO(n)–CuO(p), SnO$_2$(n)–CuO(p), SnO$_2$(n)–ZnO(n) composites showed enhanced sensitivities from single phase materials[10,11] CdO–ZnO, SnO$_2$–ZnO, SnO$_2$–In$_2$O$_3$, WO$_3$–ZnO, CuO–NiO, In$_2$O$_3$–ZnO[12–17] have been previously reported to be promising sensitive and

selective gas sensors. Surface modification of semiconductors can be achieved by the addition of a second component and used as active sites for redox processes and as promoting free charge carriers that increases the electronic conductance of oxide film.[18] Semiconductor-based heterostructure nanocomposites have received the most attention due to their excellent optical, electrical properties, photocatalytic activity,for lithium-ion battery electrodes, to detect the freshness of dead fishes and high gas sensitivity applications.[19–25] Among all these composites SnO_2–ZnO nano-composite shows great gas response to various and reducing gases because SnO_2 and ZnO both are well known n-type semiconductors with wide direct band gap Eg = 3.6 and 3.37 eV at 30,0 K respectively. Sensitivity of n-type semiconductors towards reducing gases is increased with increase in temperature.[26] The sensitivity (S) can be defined as Ra/Rg for reducing gases or Rg/Ra for oxidizing gases, where Ra stands for the resistance of gas sensors in the reference gas (usually the air) and Rg stands for the resistance in the reference gas containing target gases. Both Ra and Rg have a significant relationship with the surface reactions taking place.[27,28] Apart from this, synthesizing method is also very important preparative parameter to enhance the surface modification. In the same way various methods were developed earlier to develop homogenous, and uniform well adhered thin film. Hydrogen, hydrogen sulfide, aAmmonia, LPG, ethanol, methanol, xylene, toluene, acetone, etc., are the reducing gases. Depending upon their properties response towards semiconducting solid-state gas sensor responses differently.

In the present work, we have synthesized SnO_2–ZnO nano-composite by the Chemical Bath Deposition (CBD) method. Composition variations of SnO_2 and ZnO on structural morphological, compositional and optical properties are investigated by means of XRD, SEM, EDS and, PL analysis. After, the gas sensing behaviors of the annealed samples were tested for four different test gases, viz. LPG, ethanol, ammonia and, hydrogen sulfide. Operating temperature sensitivity, selectivity, response time and recovery time were studied for each sample and these composite materials compared with pure SnO_2 and pure ZnO annealed sample.

EXPERIMENTAL

This work involves a synthesis of SnO_2–ZnO nano-composite by the simple and inexpensive CBD method. At first, glass substrates were washed with the same procedure as mentioned in our previous work.[13] Afterward, 150 ml solutions of 0.1 M stannic cChloride ($SnCl_4$) and 0.1 M zinc chloride ($ZnCl_2$) were prepared. Then Triethanolamine solution was added dropwise in both solutions. Subsequently, three separate composite solution baths of appropriate ratio 3:1, 1:1 and 1:3

were prepared. Further, these solutions were supersaturated with the help of sodium hydroxide (NaOH) solution, then a clear transparent solution was obtained. In the same way, pure $ZnCl_2$ pure $SnCl_4$ solution bath were also prepared for the comparison and named as ZZ and SS. Finally, a white colored deposition was obtained on glass substrates after 48 h. These films were air dried for 2 h. and further subjected for annealing at temperature 500°C for 1 h. and coded as SZ1, SZ2, SZ3, SS and ZZ, respectively. These annealed films were applied to study the structural, surface morphological, compositional properties with the help of an x-ray diffractometer, Scanning Electron Microscopy (SEM), Energy Dispersive x-ray Analysis (EDS) and Photoluminescence spectroscopy (PL), etc. The gas sensing properties of synthesized films were studied using an arrangement schematically explained in our previous paper.[28] The electrical resistance of films in an air (Ra) and in the presence of test gas (Rg) was measured to evaluate the gas response, S, defined as follows,
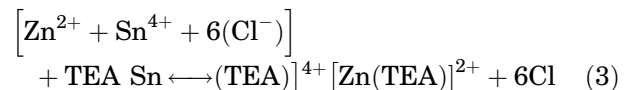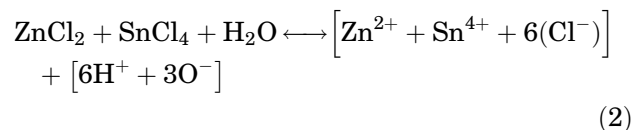
$$S(\%) = \frac{Ra - Rg}{Ra} \times 100. \tag{1}$$

RESULT AND DISCUSSION

Formation Mechanism

The synthesis of SnO_2–ZnO nano-composite by CBD involves two step nucleation, and particle growth.[29] First step nucleation of molecular clusters resulted in the homogenous film by heterogeneous reactions at the substrate surface. Nucleation steps of sample SZ1, SZ2 and SZ3 are shown in Eqs. 2, 3 and 4. The second step is annealing to remove water content and also for nanoparticle growth as shown in Eq. 5. Similarly, a reaction mechanism occurs for pure samples SS and ZZ as shown in Eqs. 6, 7, 8, 9, 10, 11, 12, and 13. In a similar manner, the whole schematic illustration of a formation process of SnO_2–ZnO nano-composite is shown in Fig. 1. It shows synthesis, film deposition and annealing process of samples SS, SZ1, SZ2, SZ3, and ZZ and finally particle growth occurs which resulted in their respective morphologies through the path (a), (b), (c), (d) and (e).

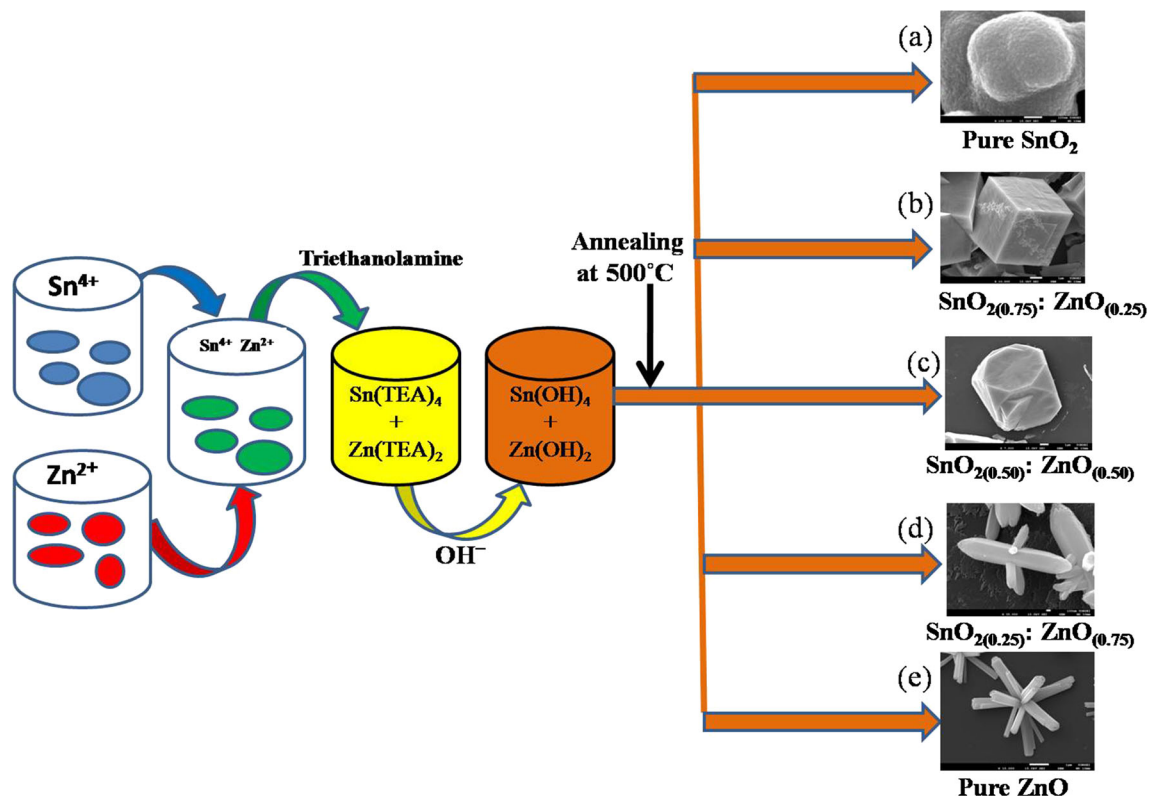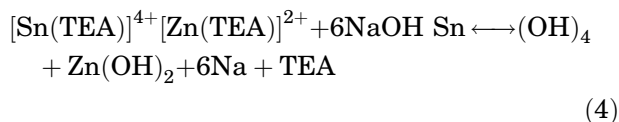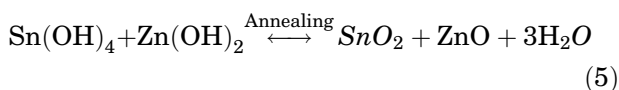Synthesis reaction mechanism of SnO_2–ZnO nanocomposite

Step I

$$\begin{aligned} ZnCl_2 + SnCl_4 + H_2O &\longleftrightarrow \left[Zn^{2+} + Sn^{4+} + 6(Cl^-) \right] \\ &+ \left[6H^+ + 3O^- \right] \end{aligned} \tag{2}$$

$$\begin{aligned} &\left[Zn^{2+} + Sn^{4+} + 6(Cl^-) \right] \\ &+ TEA\ Sn \longleftrightarrow (TEA) \big]^{4+} [Zn(TEA)]^{2+} + 6Cl \quad (3) \end{aligned}$$

Fig. 1. Schematic illustration of the formation process of pure and SnO_2–ZnO nano-composite.

$$[Sn(TEA)]^{4+}[Zn(TEA)]^{2+}+6NaOH\ Sn \longleftrightarrow (OH)_4 + Zn(OH)_2+6Na + TEA$$

$$(4)$$

Step II

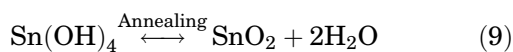$$Sn(OH)_4+Zn(OH)_2 \overset{Annealing}{\longleftrightarrow} SnO_2 + ZnO + 3H_2O$$

$$(5)$$

Synthesis reaction Mechanism of pure SnO_2
Step I
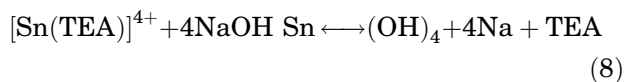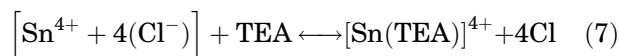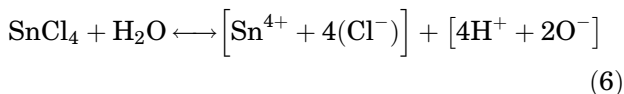
$$SnCl_4 + H_2O \longleftrightarrow \left[Sn^{4+} + 4(Cl^-)\right] + \left[4H^+ + 2O^-\right]$$

$$(6)$$

$$\left[Sn^{4+} + 4(Cl^-)\right] + TEA \longleftrightarrow [Sn(TEA)]^{4+}+4Cl \quad (7)$$

$$[Sn(TEA)]^{4+}+4NaOH\ Sn \longleftrightarrow (OH)_4+4Na + TEA$$

$$(8)$$

Step II

$$Sn(OH)_4 \overset{Annealing}{\longleftrightarrow} SnO_2 + 2H_2O \qquad (9)$$
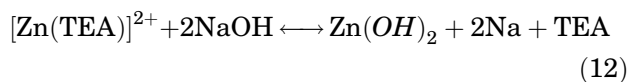
Synthesis reaction Mechanism of SnO_2–ZnO nanocomposite
Step I

$$ZnCl_2 + H_2O \longleftrightarrow \left[Zn^{2+} + 2(Cl^-)\right] + \left[2H^+ + O^-\right]$$

$$(10)$$

$$\left[Zn^{2+} + 2(Cl^-)\right] + TEA \longleftrightarrow [Zn(TEA)]^{2+}+2Cl \quad (11)$$

$$[Zn(TEA)]^{2+}+2NaOH \longleftrightarrow Zn(OH)_2 + 2Na + TEA$$

$$(12)$$

Step II

$$Zn(OH)_2 \overset{Annealing}{\longleftrightarrow} ZnO + H_2O \qquad (13)$$
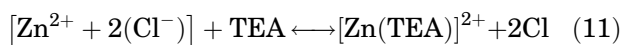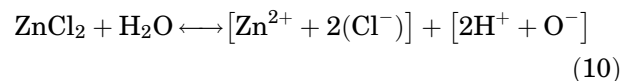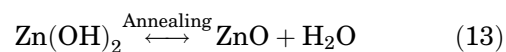
X-ray Difraction

The structural changes and identification of phases of SnO_2 thin films obtained by CBD are investigated with the help of x-ray diffraction (XRD). The synthesized sample was characterized by a Philips automated x-ray diffractometer (PW-3710) equipped with a crystal monochromator employing Cu–Kα radiation of wavelength 1.5406 A°. The diffracting angle (2θ) is varied between 20°
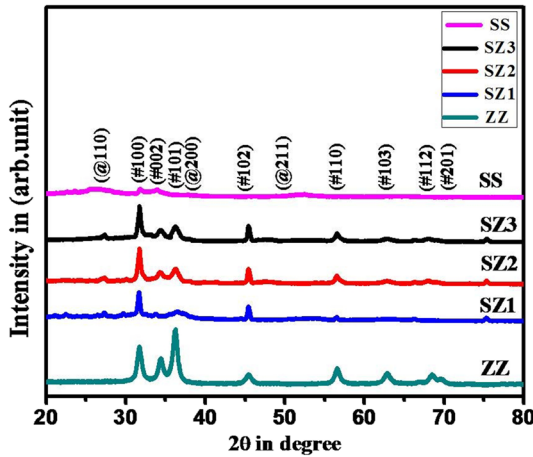
Fig. 2. Powder x-ray diffraction patterns of SnO_2 (SS), $SnO_{2(0.75)}$–$ZnO_{(0.25)}$ (SZ1), $SnO_{2(0.50)}$–$ZnO_{(0.50)}$ (SZ2), $SnO_{2(0.75)}$–$ZnO_{(0.25)}$ (SZ3) and ZnO (ZZ).

Fig. 3. (a) Scanning electron microscope images of (a1)–(a3) SnO_2 (SS); (b1)–(b3) $SnO_{2(0.75)}$–$ZnO_{(0.25)}$ (SZ1), (c1)–(c3) $SnO_{2(0.50)}$–$ZnO_{(0.50)}$ (SZ2), (d1)–(d3) $SnO_{2\ (0.25)}$ –$ZnO_{(0.75)}$ (SZ3) and (e1)–(e3) ZnO (ZZ) (b) Magnified scanning electron microscope images of (B), (C) and (D) of sample (SZ1), (SZ2) and (SZ3) along with dimensions, respectively.

and 80° and the recorded XRD patterns for the thin films are shown in Fig. 2. The annealed SS sample showed major peaks at $2\theta = 26.42°$, 33.4°, 37.6°, and 52.1° which correspond to planes of (110), (101), (200) and (211) respectively (matches with JCPDS file no. 41-1445).[16] No obvious reflection peaks from impurities such as unreacted Sn or SnO were detected, and there are no secondary phases present, thus indicating that high purity of the product with a tetragonal rutile structure. XRD pattern for the sample SZ1, SZ2 and SZ3 exhibits the mixed phases of SnO_2 and ZnO. It is also observed that an addition of ZnO to composite samples might enforce the formation of crystal along 1-dimension which reflects in growth of intensity for the (100) plane from composite SZ1 to SZ3. XRD pattern obtained from the SnO_2–ZnO composite structure showed additional peaks besides tetragonal rutile SnO_2 peaks at 31.81°, 34.54°, 36.29°, 47.53°, 56.58°, 62.85° and 67.92° which corresponds to (100), (002), (101), (102), (110), (103) and (112) planes, respectively, of hexagonal wurtzite crystal structure of ZnO (match with the [JCPDS file No.36-1451]). Also, due to an increase in disorder strain developed in the sample, peak broadening is observed from SZ1 to SZ3.

SEM and EDS

Scanning Electron Microscopy (SEM) micrographs of SnO_2, ZnO, and the SnO_2–ZnO nanocomposite films are shown in Fig. 3a. The morphology of the annealed samples was measured by Field-Emission Scanning Electron Microscopy (FESEM, JSM-7001F, JEOL). Scanning electron microscope images of (a1)–(a3) pure SnO_2 (SS) shows interconnected nanospheres morphology. However, (b1)–(b3) SnO₂:0.75–ZnO:0.25 (SZ1), (c1)–(c3) SnO₂:0.50–ZnO:0.50 (SZ2), (d1)–(d3) SnO₂:0.25 – ZnO:0.75 (SZ3) and (e1) to (e3) pure ZnO shows nano-cubes, hexagonal nano-dice and manifold

hexagonal nano-rod and hexagonal nano-rod like morphology, respectively. Such morphological structures are useful in gas sensor applications.[30,31] It is observed that the addition of ZnO to SnO_2 converts morphology from nano-cubes to hexagonal nano-rods as ZnO facilitates one-dimensional crystal growth which is observed from XRD also.

In Fig. 3b, SEM image (G), (J) and (M) shows magnified SEM images along with their dimensions of a sample (SZ1), (SZ2) and (SZ3), respectively. The $(SnO_2)_{1-X}ZnO_X$ sample with X = 0.25, 0.50 and 0.75 shows development of nano-cubes, nano-dice and manifold hexagonal nano-rods which have grown over a complete glass substrate. These SEM images are observed at resolution of x 10,000, x 8000 and x 35,000, respectively, at constant voltage 15.0 kV. In Fig. 3b of image (G) of the sample SZ1 nano-cube has observed dimensions that are $3.90 \times 4.52 \times 4.99$ μm, i.e., of average ~ 4.47 μm in length. Similarly in the image (J) of sample SZ2 hexagonal dice has observed dimensions of average ~ 2.8 μm in length and that of an image (M) hexagonal rod has an observed dimension in length of 2.72 μm and its manifolds have an average length of ~ 650 nm. Such a change in morphology generates due to the different ZnO content in the SnO_2. However, such types of morphologies are useful in gas sensor applications because they form a path of an electron channel through interconnected cubes, dice or manifold rods and such interconnected structure forms an interconnected web network.

Elemental composition is confirmed by Energy Dispersive x-ray Spectroscopy (EDS). From Fig. 4 and Table I show that tin, zinc, and oxygen are the major constituents of the film. These constituents show their intensity according to their percentage present in the film. However, in sample SZ1 to SZ3 there are two major unlabeled peaks at the lower end. Those peaks at the lower end correspond to the carbon, and the intensity of the signal is quite considerably high. These signals correspond to the carbon and originated from carbon tape during characterization of EDS spectra, since carbon tape was used for support and sink for the excess electrons. The percentage of tin in the composite sample decreases from SZ1 to SZ3. It is observed that in Fig. 3a with the change in composition, the morphology of the sample changes accordingly.

Photoluminescence

Figure 5 shows photoluminescence (PL) spectra for sample SS, ZZ, SZ1, SZ2, and SZ3 were investigated at room temperature. The results indicate
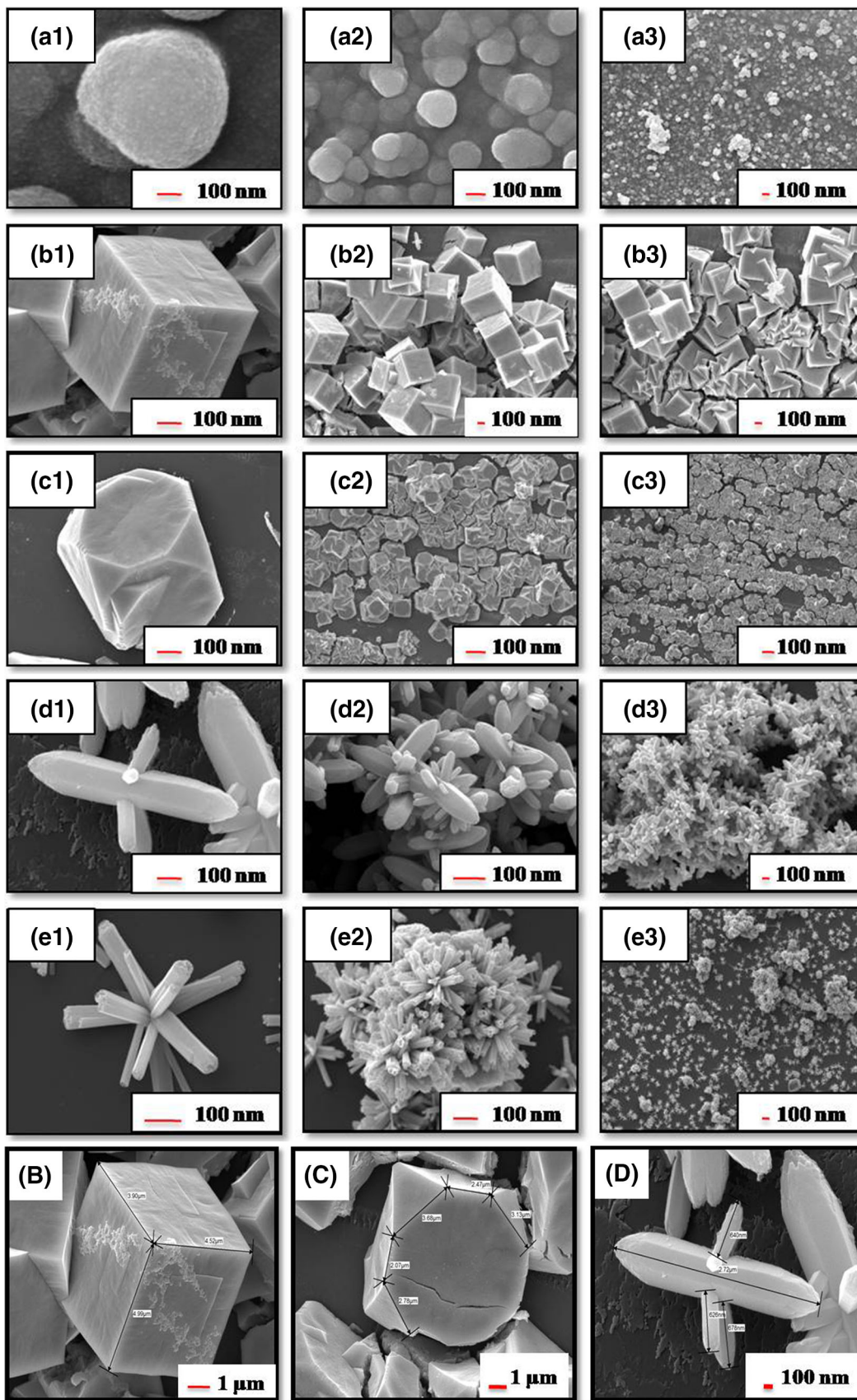
that the response of the PL spectra has two emitting bands including a weak emission band in the (Ultraviolet) UV region. Generally visible spectrum observed is associated with structural defects. Maximum intensity was observed for SS 360 nm (3.44 eV), SZ1 368 nm (3.36 eV), SZ2 354 nm, (3.50 eV), and SZ3 350 nm (3.54 eV) a strong
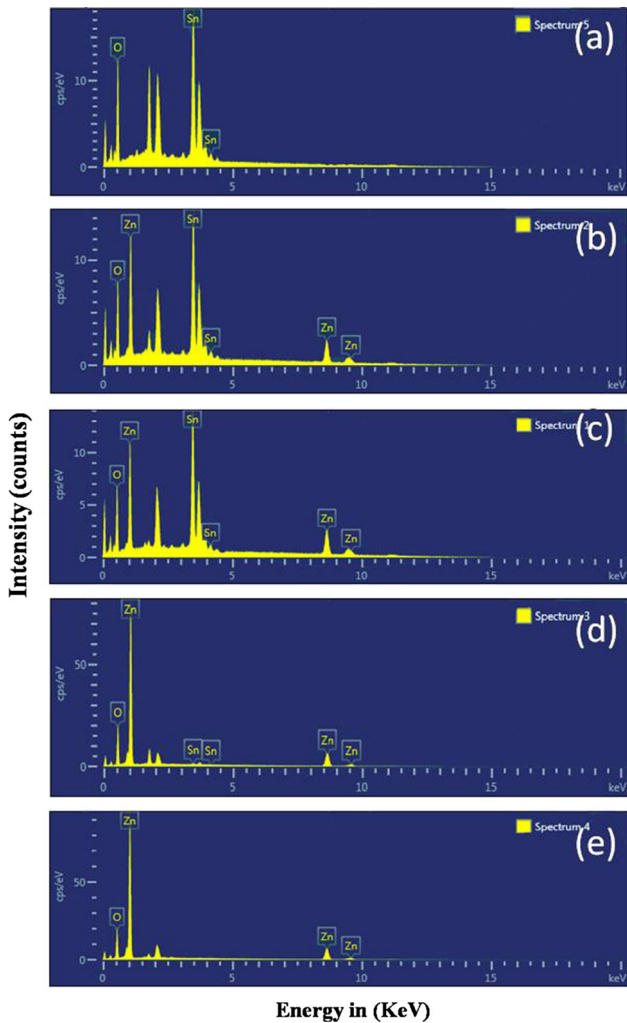
emission band in the visible region for sample SS, ZZ, SZ1, SZ2, and SZ3. The band gap energy of nanocomposite samples SZ1, SZ2 and SZ3 were increasing, as observed from Fig. 5. The UV emission band originates from the direct recombination of the free excitons through an exciton–exciton collision process, while the emission peaks are due to radial recombination of the photo-generated hole with the electrons that belong to the singly ionized oxygen vacancies.[19,32]

GAS SENSING STUDIES

As per the present scenario, present work is mainly focused on composite material owing to their complementary action to each other. Also, high sensing performance can be noted due to modification of barrier potential at the interface. The composite film shows better sensing response as compared with pure oxide film, which is shown in Table II.[33–37]

As the operating temperature is the essential parameter for characterizing the sensor, SnO_2–ZnO films were employed to obtain optimum operating temperature. Figure 6a–e shows the gradual increase in the response of the sensor and reaches its maximum value and then decreases with respect
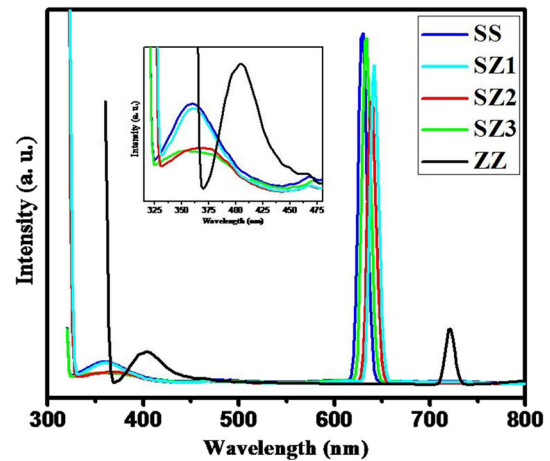

Fig. 4. EDS spectrum of sample (1) Pure SnO_2 (SS) (2) $SnO_{2(0.75)}$–$ZnO_{(0.25)}$ (SZ1), (3) $SnO_{2\ (0.50)}$–$ZnO_{(0.50)}$ (SZ2), (4) $SnO_{2(0.25)}$–$ZnO_{(0.75)}$ (SZ3) and (5) Pure SnO_2 (ZZ).

Fig. 5. PL spectra for sample SS, SZ1, SZ2 SZ3 and ZZ and inset showing enlarged UV absorption band of same.

Table I. Elemental analysis of sample SS, SZ1, SZ2 and SZ3 by EDS

Sample name	Atomic wt%				
	ZZ	SZ1	SZ2	SZ3	SS
O	54.02	64.29	66.00	56.78	80.43
Sn	–	17.92	16.55	0.59	19.57
Zn	45.98	17.79	17.44	42.62	–
Total	100	100	100	100	100

Table II. Ethanol sensors based on SnO$_2$ materials reported before and SnO$_2$–ZnO in present work

Sr. no	Material	Sensitivity	Concentration (ppm)	Operating temp. (°C)	References
1	SnO$_2$	20.1	100	280	33
2	SnO$_2$	∼7	800	300	34
3	SnO$_2$	30.7	100	300	35
4	SnO$_2$	24.9	100	300	36
5	SnO$_2$	∼57	250	400	37
6	SnO$_2$–ZnO	59.67	24	275	[Present work]

to operating temperature. Such behavior can be explained by the kinetics and mechanics of gas reaction which occurred on the surface.[38] For low and high temperatures the sensor response is confined by the speed of chemical reactions and speed of the diffusion of gas molecules to that surface, respectively.[39] The sensing behavior for different gases is shown in Fig. 6a–d. The SnO$_2$–ZnO sensor exhibits a higher response at lower operating temperature and the lower concentration of 24 ppm target gas. It can be credited to the formation of n–n heterojunction at intergrain boundaries of SnO$_2$–ZnO composite. Also, it is evident from Fig. 6e that sample SZ2 exhibits higher response towards ethanol gas (59.67%) in comparison with LPG, (51.88%), ammonia (NH3) (48.57%) and hydrogen sulfide (H$_2$S) (47.24%) at an operating temperature of 275°C. Consequently, SnO$_2$–ZnO sensor showed selectivity towards ethanol against LPG, ammonia and hydrogen sulfide.

Furthermore, Fig. 7a indicates that the ethanol gas response of SnO$_2$–ZnO (Sample SZ2) sensor is higher than that of pure sample ZZ and SS sensor under the same concentration. Similarly, SZ2 sample responses effectively compared with sample SS and ZZ to other test gases in Fig. 7b and c.

Similarly, it is noted that Fig. 8 shows the responses increase with increasing concentration of test gases. As in Fig. 8, it is observed that at 12 ppm concentration of ethanol gas 15.68% response was observed and that of 24 ppm concentration of ethanol 59.67% response was observed. On the other hand, the same type of behavior was observed in other test gases such as LPG, ammonia and hydrogen sulfide. So it was pragmatic that the gas concentration affects test gas response at constant operating temperature. Figure 9 revealed nature of response and recovery time of sample SZ2. It is observed that recovery time of gas goes on increases with respect to increase in gas concentration while that of response time decreases with respect to concentration of gas.

Sensing Mechanism

Sensing mechanism for of *n*-type semiconducting is merely dependent upon the widely accepted theory of exchange of electrons between the sensor surface and chemisorbed species that modify the surface conductivity of the sensor.[40,41] When the sensing material is exposed to target gases (such as LPG, ethanol, ammonia and hydrogen sulfide), the reaction between gas molecules and adsorbed oxygen molecules will take place. It releases electrons back to the conduction band of materials. These electrons recombine with holes, which increases the electrical conductivity of the semiconductor. In our study composite sensors show better selective response towards ethanol as compared with other test gases. This might be due to the different reaction mechanism of ethanol with the oxide surface. *Jinkawa* et al. reported that decomposition of ethanol at elevated temperatures depends on the acid–base properties of the oxide material. Also, the addition of basic material increases the response to ethanol by approximately 10-40 times at 1000 ppm concentration.[42] Ethanol molecule may undergo a different reaction, i.e., dehydration and dehydrogenation.[43,44] Those reactions are mentioned as (14) and (15). The intermediate CH$_3$CHO and C$_2$H$_4$ can react with oxygen ions to produce CO$_2$ and H$_2$O as mentioned in Eqs. 16 and 17.

In dehydrogenation and dehydration reaction CH$_3$CHO and C$_2$H$_4$ intermediates were formed, respectively.[13,45] In the present study, SnO$_2$ is acidic in nature while ZnO is basic. Hence, the addition of ZnO increases the basicity of the composite sensor which favors the dehydrogenation of ethanol to CH$_3$CHO + H$_2$O with the negatively charged surface oxygen (O$_{surf}^-$) which induces a larger increase in conductance than that of C$_2$H$_4$. However, our sample SZ2 has more proportion of ZnO. Hence, sample SZ2 is more responsive towards ethanol.

On the other hand, LPG is more responsive towards sample SZ2 at temperature 275°C, but its
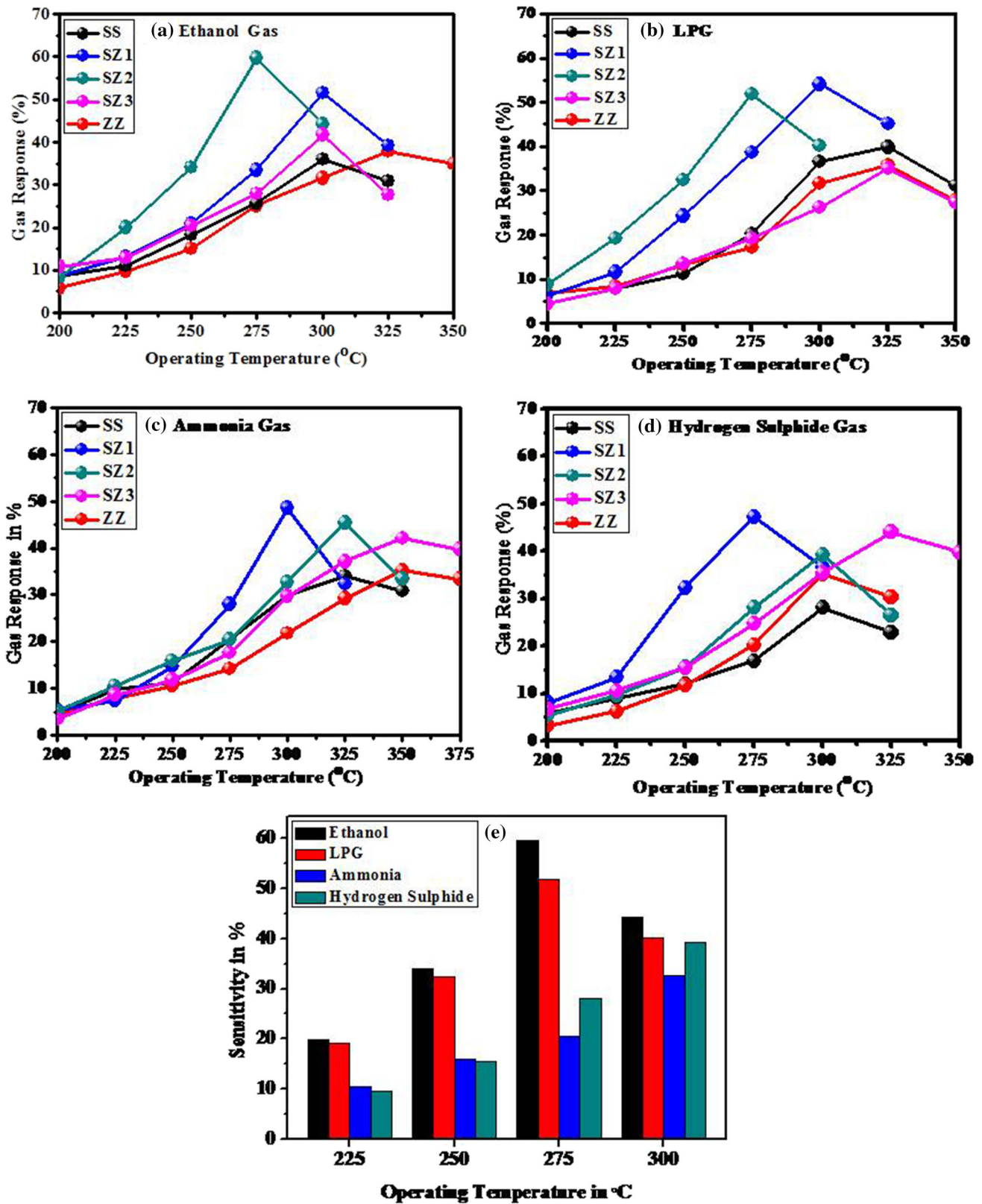
Fig. 6. (a-d) Plot of gas response as a function of operating temperature for different samples (SS, SZ1, SZ2, SZ3 and ZZ) for (a) Liquefied petroleum gas (b) ethanol, (c) ammonia gas and (d) hydrogen sulfide, to 24 ppm of respective gases. (e) Bar chart showing different test gases response with respect to operating temperature.
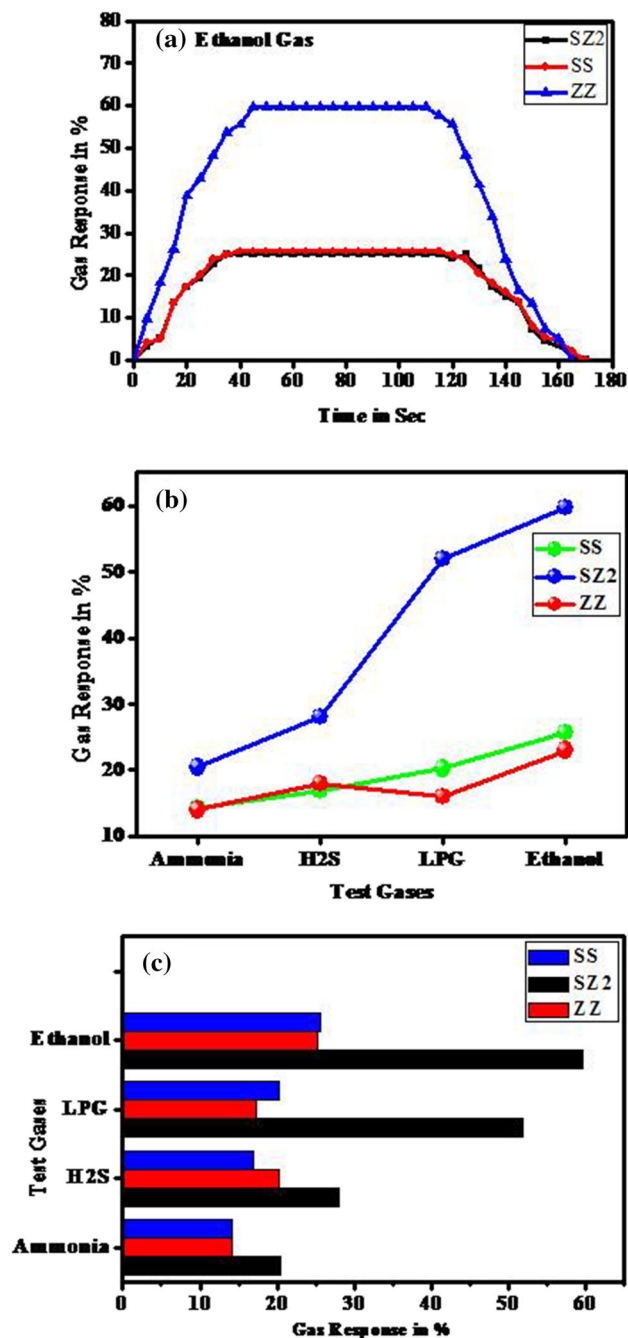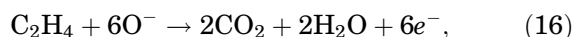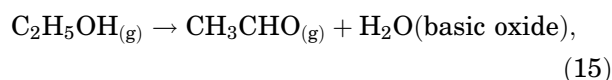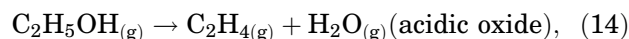
Fig. 7. (a) Transient gas response of sample SS, SZ2 and ZZ at 275°C for ethanol to 24 ppm (b) Transient gas response of sample SS, SZ2 and ZZ at for four different test gases at 24 ppm gas concentration and (c) Bar graph of a graph (b).
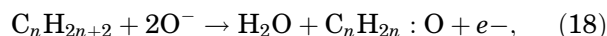
maximum response is recorded by sample SZ1 at temperature 300°C. Similarly, for ammonia and hydrogen sulfide gases, the maximum gas response

is recorded for sample SZ1. Sample SZ1 has more proportion of SnO$_2$ which is favorable for sensing LPG, H$_2$S and NH$_3$ gases.[46–48] Therefore, the proportions of SZ1 and SZ2 significantly affect the gas response. Further, the reactions of other test gases with composite sensors are shown in Eqs. 18, 19, 20 and 21 respectively.
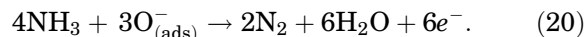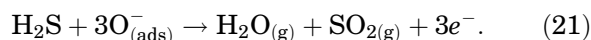
Reaction of ethanol

$$C_2H_5OH_{(g)} \rightarrow C_2H_{4(g)} + H_2O_{(g)}(\text{acidic oxide}), \quad (14)$$

$$C_2H_5OH_{(g)} \rightarrow CH_3CHO_{(g)} + H_2O(\text{basic oxide}), \quad (15)$$

$$C_2H_4 + 6O^- \rightarrow 2CO_2 + 2H_2O + 6e^-, \quad (16)$$

$$2CH_3CHO + 5O^- \rightarrow 4CO_2 + 2H_2O + 5e^-. \quad (17)$$

Reaction of LPG

$$C_nH_{2n+2} + 2O^- \rightarrow H_2O + C_nH_{2n} : O + e-, \quad (18)$$

$$C_nH_{2n} : O + O^- \rightarrow CO_2 + H_2O + e^-. \quad (19)$$

(Here C$_n$H$_{2n+2}$ represents CH$_4$, C$_3$H$_8$, C$_4$H$_{10}$, etc., and C$_n$H$_{2n}$: O partially oxidized intermediate on the surface).

Reaction of ammonia

$$4NH_3 + 3O^-_{(ads)} \rightarrow 2N_2 + 6H_2O + 6e^-. \quad (20)$$

Reaction of H$_2$S

$$H_2S + 3O^-_{(ads)} \rightarrow H_2O_{(g)} + SO_{2(g)} + 3e^-. \quad (21)$$

It may be noted that the quantity of adsorbed intermediates is more dominant compared with LPG, ammonia and hydrogen sulfide. In addition, the reaction between ethanol and adsorbed oxygen releases more electrons under the same time span, and; thus, it may cause shorter response time and improved response. Furthermore, composite SZ2 exhibits better sensing characteristics than pure sample SS and ZZ. This might be due to the formation of heterocontact between SnO$_2$ and ZnO and electron transfer from SnO$_2$ to ZnO due to their work function difference. As a result, electrostatic potential energy on both side changes and subsequently lowering of barrier height takes place which causes a significant change in resistance. Thus, enhancement in sensing performance is noted.
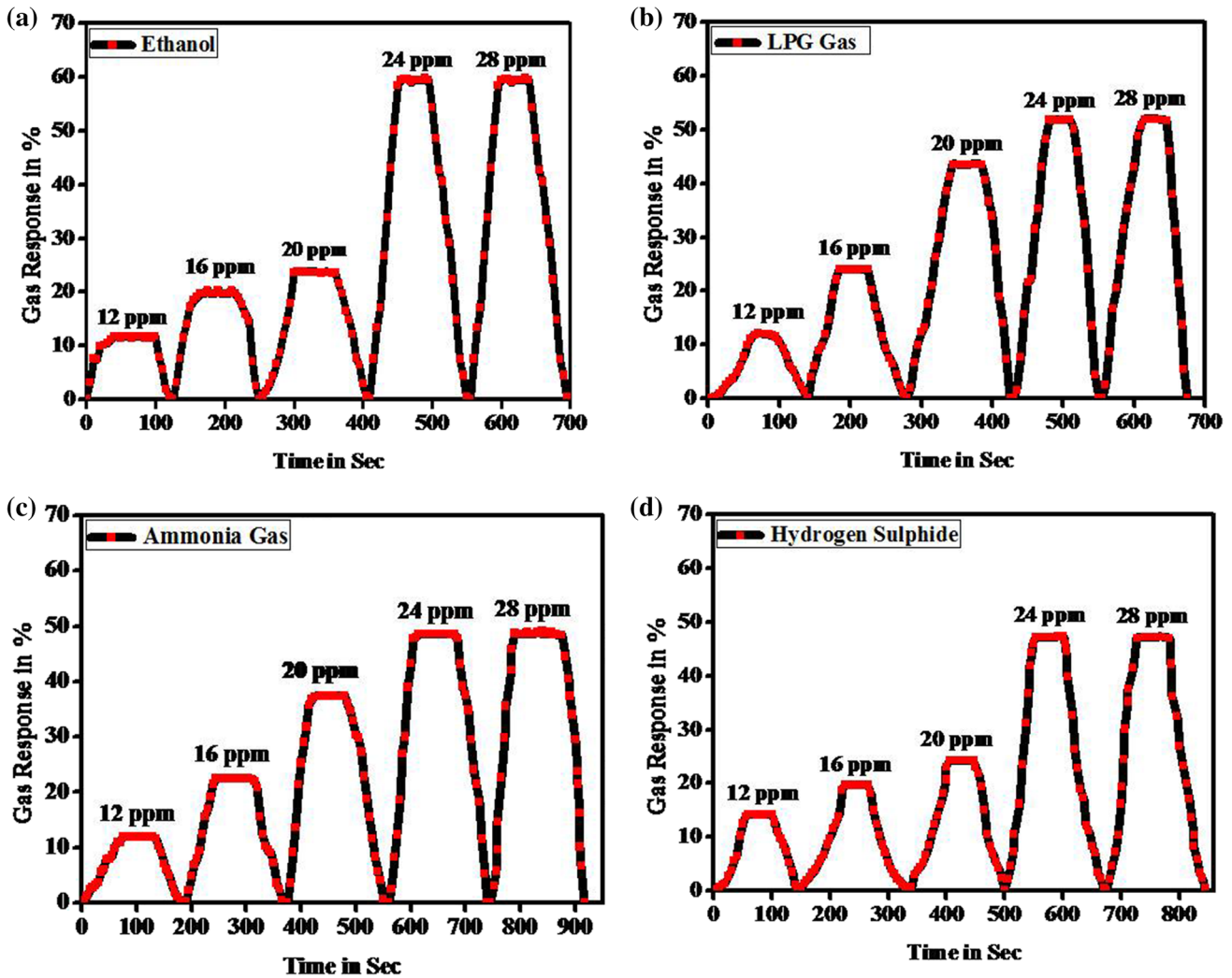
Fig. 8. Response under different gas concentration for (a) ethanol, (b) LPG (c) ammonia, (d) hydrogen sulfide at their respective operating temperature.
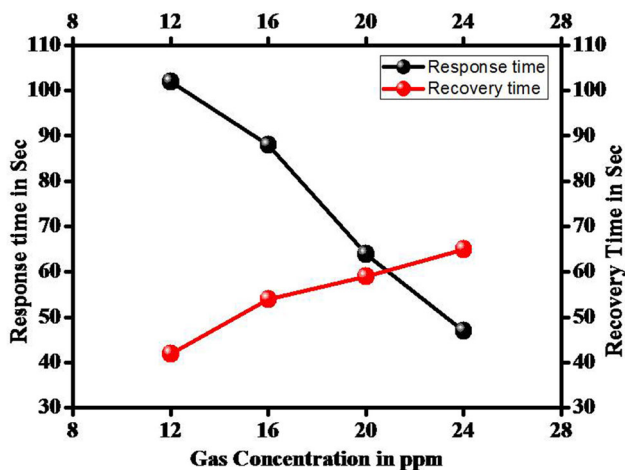

Fig. 9. Graph of response and recovery time correlation with respect to ethanol gas concentration in ppm.

So finally, we conclude that ethanol gas is responsive towards SZ2 sample and except ethanol, all the other three gases show the greater response for sample SZ1, such response might be observed due to change in material proportion.

CONCLUSION

CBD method was successfully applied for synthesis of SnO_2–ZnO nanocomposite. XRD confirms that composite samples are polycrystalline in nature whereas pure SnO_2 and pure ZnO showed tetragonal rutile and hexagonal wurtzite crystal structure, respectively. SEM analysis revealed the development of interconnected nano-sphere, nano-cubes, nano-dice, manifold nano-rods and hexagonal nano-rod like morphology for samples SS, SZ1, SZ2, SZ3, and ZZ respectively. Elemental compositions were confirmed by EDS analysis. SnO_2–ZnO composite

sample SZ2 sensor showed the highest response with shorter response time compared with pure sample SS and ZZ sensors. The SnO$_2$–ZnO composite sample SZ2 sensor showed a maximum response of 59.67% to 24 ppm of ethanol. Thus, SnO$_2$–ZnO composite sensor is selective towards ethanol against LPG, ammonia and hydrogen sulfide, even at a lower concentration.

REFERENCES

1. S. Yan, S. Ma, W. Li, X. Xu, L. Cheng, H. Song, and X. Liang, *Sens Actuators B Chem.* 221, 88 (2015).
2. N. Yamazoe, *Sens Actuators B Chem.* 108, 2 (2005).
3. K. Jeevitesh, T. Rajput, K. Pathak, V. Kumar, H. Swart, and L. Purohit, *Physica B Condens Matter.* 535, 314 (2018).
4. D. Han, L. Zhai, F. Gu, and Z. Wang, *Sens Actuators B Chem.* 262, 655 (2018).
5. D. Dao, K. Shibuya, T. Bui, and S. Sugiyama, *Procedia Eng.* 25, 1149 (2011).
6. Y. Hou and J. Ahalapatiya, *Proc. Nat.l Sci. Mater.* 27, 435 (2017).
7. R. Zhao, Z. Wang, Y. Yang, X. Xing, T. Zou, Z. Wang, and Y. Wang, *J. Phys. Chem. Solids* 120, 173 (2018).
8. Z. Li, X. Niu, Z. Lin, N. Wang, H. Shen, W. Liu, K. Sun, Y. Fu, and Z. Wang, *J. Alloys Compd.* 682, 647 (2016).
9. D. Patil, V. Patil, and P. Patil, *Sens Actuators B Chem.* 152, 299 (2011).
10. M. Saha, A. Banargy, A. Haldar, J. Mondal, A. Sen, and H. Maiti, *Sens Actuators B Chem.* 79, 192 (2001).
11. N. Yamada, Y. Kurokawa, and T. Seiyama, *Sens Actuators B Chem.* 4, 283 (1983).
12. A. Sharma, S. Potdar, K. Pakhare, B. Sargar, M. Rokade, and N. Tarwal, *J. Mater. Sci.: Mater. Electron.* 28, 3752 (2017).
13. W. Li, S. Ma, Y. Li, G. Yang, Y. Mao, J. Luo, D. Gengzang, X. Xu, and S. Yan, *Sens Actuators B Chem.* 211, 392 (2015).
14. C. Aifan, H. Xiaodong, T. Zhangfa, B. Shouli, L. Ruixian, and L. Chiun, *Sens Actuators B Chem.* 115, 316 (2006).
15. Y. Liu, J. Yu, and P. Lai, *Int. J. Hydrogen Energy* 39, 10313 (2014).
16. Y. Wang, F. Qu, J. Liu, Y. Wang, J. Zhou, and S. Ruan, *Sens Actuators B Chem.* 209, 515 (2015).
17. M. Gholami, A. Khodadadi, A. Firooz, and Y. Mortazavi, *Sens Actuators B Chem.* 212, 395 (2015).
18. S. Hemmati, A. Firooz, A. Khodadadi, and Y. Mortazavi, *Sens Actuators B Chem.* 160, 1298 (2011).
19. J. Wang, Z. Chena, Y. Liu, C. Shek, C. Wu, and J. Lai, *Sol. Energy Mater. Sol. Cells* 128, 254 (2014).
20. J.-C. Li, X. Hou, and Q. Cao, *J. Alloys Compd.* 611, 219 (2014).
21. M. Ahmad, S. Yingying, H. Sun, W. Shen, and J. Zhu, *J. Solid State Chem.* 196, 326 (2012).
22. W. Wang, Y. Zhu, and L. Yang, *Adv. Funct. Mater.* 17, 59 (2007).
23. W. Zhang and W. Zhang, *Sens Actuators B Chem.* 134, 403 (2008).
24. C. Liangyuan, B. Shouli, Z. Guojun, L. Dianqing, C. Aifan, and C. Liu, *Sens Actuators B Chem.* 134, 360 (2008).
25. A. Sharma, S. Potdar, M. Yewale, D. Shirgaonkar, K. Pakhare, B. Sargar, M. Rokade, and U. Patil, *Mater. Sci.* 37, 1 (2019).
26. X. Liu, S. Cheng, H. Liu, S. Hu, D. Zhang, and H. Ning, *Sensors* 12, 9635 (2012).
27. C. Wang, L. Yin, L. Zhang, D. Xiang, and R. Gao, *Sensors* 10, 2088 (2010).
28. K. Pakhare and B. Sargar, *Int. J .Curr. Eng. Sci. Res.* 4, 84 (2017).
29. A. Kohan, G. Cender, D. Morgan, and C. Walle, *Phys. Rev. B* 61, 15019 (2000).
30. N. Md Sin, M. Mamat, M. Malek, and M. Rusop, *Appl. Nanosci.* 4, 829 (2014).
31. S. Wanga, W. Yub, C. Chenga, T. Zhangb, M. Gec, Y. Sunb, and N. Daib, *MRS Bull.* 89, 267 (2017).
32. S. Wang, W. Yu, C. Cheng, T. Zhang, M. Ge, Y. Sun, and N. Dai, *MRS Bull.* 89, 267 (2017).
33. Z. Lou, L. Wang, R. Wang, T. Fei, and T. Zhang, *Solid State Electron.* 76, 91 (2012).
34. M. Kumara, A. Kumarb, and A. Abhyankar, *Ceram. Int.* 40, 8411 (2014).
35. S. Santra, A. Sinha, A. Luca, S. Ali, F. Udrea, P. Guha, S. Ray, and J. Gardner, *Nanotechnology* 27, 125502 (2016).
36. X. Wang, P. Ren, H. Tian, H. Fan, C. Cai, and W. Liu, *J. Alloy. Compd.* 669, 29 (2016).
37. Y. Li, *Physica E Low Dimens. Syst. Nanostruct.* 96, 54 (2018).
38. L. Liu, S. Li, J. Zhuang, L. Wang, J. Zhang, and H. Li, *Sens Actuators B Chem.* 155, 782 (2011).
39. T. Nenov and S. Yordanov, Ceramic sensor- technology and applications, (Technomic Publishing: Lancaster, P, USA, 1996).
40. L. Cheng, S. Ma, X. Li, J. Luo, W. Li, F. Li, Y. Mao, T. Wang, and Y. Li, *Sens Actuators B Chem.* 200, 181 (2014).
41. K. Pakhare, B. Sargar, S. Potdar, and A. Sharma, *Int. J. Eng. Res. Appl.* 7, 6 (2017).
42. T. Jinkawa, G. Sakai, J. Tamaki, N. Miura, and N. Yamazoe, *J. Mol. Catal. A: Chem.* 155, 193 (2000).
43. J. Xu, J. Han, Y. Zang, Y. Sun, and B. Xie, *Sens Actuators B Chem.* 132, 334 (2008).
44. P. Rai and Y. Yu, *Sens Actuators B Chem.* 173, 58 (2012).
45. P. Rakshit, S. Santra, I. Manna, and S. Ray, *RSC Adv.* 4, 36749 (2014).
46. U. Nakate, P. Patil, B. Ghule, S. Ekar, A. Al-Osta, V. Jadhav, R. Mane, S. Kale, M. Naushad, and C. O'Dwyer, *J. Anal. Appl. Pyrolysis* 124, 362 (2017).
47. M. Gurbuza, G. Gunkayac, and A. Dogan, *Appl. Surf. Sci.* 318, 334 (2014).
48. Z. Song, S. Xu, M. Li, W. Zhang, H. Yu, Y. Wang, and H. Liu, *Thin Solid Films* 618, 232 (2016).